Non-fluorinated non-solvating cosolvent enabling superior performance of lithium metal anode battery

Jun yeob Moon
Seoul National University

Dong Ok Kim
Seoul National University

Lieven Bekaert
Vrije Universiteit Brussel   https://orcid.org/0000-0003-1776-1888

Munsoo Song
Seoul National University

Jinkyu Chung
Seoul National University

Danwon Lee
Seoul National University

Annick Hubin
Vrjie Universiteit Brussel

Jongwoo Lim (✉ jwlim@snu.ac.kr)
Seoul National University   https://orcid.org/0000-0002-3897-7488

Article

Non-fluorinated non-solvating cosolvent enabling superior performance of lithium metal anode battery

Junyeob Moon[1,†], Dong Ok Kim[1,2,†], Lieven Bekaert[3], Munsoo Song[1], Jinkyu Chung[1], Danwon Lee[1], Annick Hubin[3,*], Jongwoo Lim[1,*]

[1] Department of Chemistry, College of Science, Seoul National University, Seoul, 08826, Republic of Korea

[2] Department of Chemistry and Biochemistry, Swarthmore College, Swarthmore, PA 19081, United States of America

[3] Vrije Universiteit Brussel, Research Group Electrochemical and Surface Engineering, Pleinlaan 2, 1050, Brussels, Belgium

[†] These authors contributed equally: Junyeob Moon, Dong Ok Kim

[*] Corresponding authors, e-mail: annick.hubin@vub.be, jwlim@snu.ac.kr

Abstract

Lithium–ion solvation governs the performance of lithium metal anode (LMA) by tuning its interfacial stability. Solvation degree is modulated by adopting fluorinated non-solvating cosolvents (FNSC) to induce anion-rich solvation structure which is beneficial in constructing mechanically stable interface to suppress lithium dendrite. However, FNSC exhibits low cathodic stability owing to their low lowest unoccupied molecular orbital (LUMO) level, aggravating long-term cycling of LMA. We establish that spectroscopically measured Lewis basicity and polarity are critical parameters for designing optimal non-solvating cosolvents. Non-fluorinated non-solvating cosolvents (NFNSC) proposed by our design rule (i.e. anisole, ethoxybenzene and furan) delivered 99.0 % coulombic efficiency over 1400 cycles. In these molecules, the aromatic ring delocalizes oxygen electron pairs and lowers solvation capability, confirmed by electrochemical cycling, Raman spectroscopy, and DFT binding energy calculation. Finally, the quantification of remaining NFNSC in the electrolytes using nuclear magnetic resonance spectroscopy proves their reductive stability for extended cycles.

Introduction

Cosolvents are widely developed for application in a lithium–ion battery (LIB) electrolyte to enhance anion solvation[1,2], flame retardancy[3,4], lithium–ion migration[5], and high-voltage stability[6,7]. An increase in the demand for high-energy density LIB requires the development of LMA owing to the remarkably high specific energy[8,9]. However, the dendritic growth of lithium metal, which leads to the failure of the battery, remains problematic[10]. Mechanically strong interphases are reportedly effective in preventing dendrite formation[11]. Recent studies have demonstrated that the addition of a non-solvating cosolvent to generate localized high concentration electrolyte (LHCE) can induce compact lithium–ion-anion solvation pairs that participate in high-strength inorganic SEI generation [1,2 12,13].

Thus far, design strategies for ideal non-solvating cosolvents are largely unexplored and thus limited to only fluorinated non-solvating cosolvents (FNSCs) [14–16]. The negative inductive effect of fluorine withdraws electrons near the adjacent oxygen within the solvent molecules, which lowers lithium solubility[17]. Further, this decreases cathodic stability, and it results in a facile decomposition to LiF-rich SEI[18–20]. It has been largely overlooked that the accelerated decomposition to SEI consumes cosolvents, and this leads to electrolyte dry-up and battery failure[21–24]. Further, the high cost and hazardous environmental effect of FNSC necessitate the use of non-fluorinated compounds as non-solvating cosolvents[15,25,26].

In this study, we present the design rule for ideal non-solvating cosolvents, which is justified by the superior performance of non-fluorinated non-solvating cosolvents (NFNSC) that cycle over 350 cycles (99.0 %, ethoxybenzene), 500 cycles (98.5 %, anisole (AN)), and 1300 cycles (99.0 %, furan). The experimentally characterizable solvation ability and miscibility allow us

52 to identify the ideal physicochemical properties of non-solvating cosolvents. The resonating

53 electron pairs of an oxygen atom decreases the basicity of the NFNSC, thereby realizing

54 desirable non-solvating characteristics while maintaining good miscibility, superior cathodic
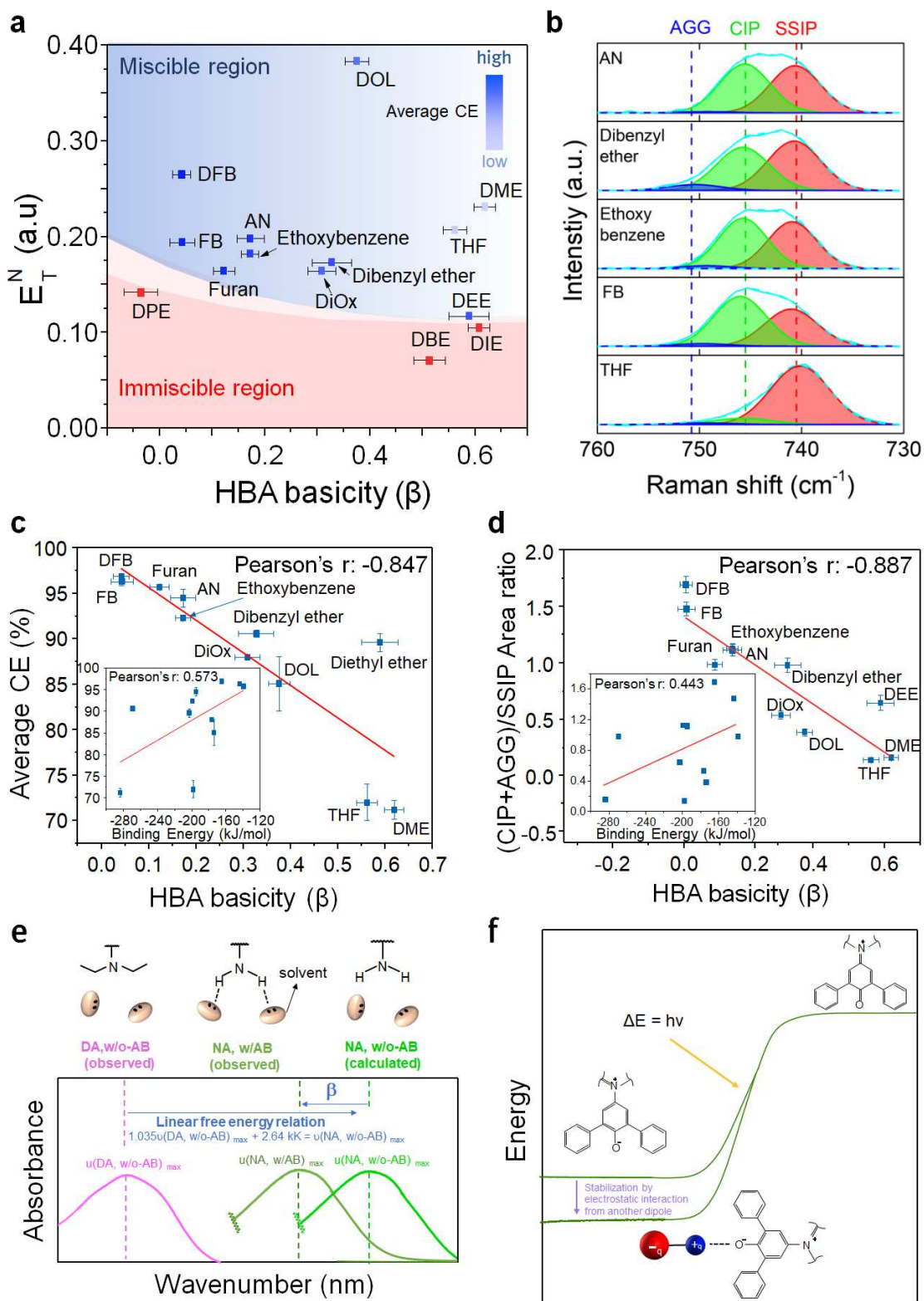
55 stability, and low price.

56

Results

58 **Physicochemical properties of NFNSC and design strategy**

59 A non-solvating cosolvent, also known as a diluent, maintains the beneficial high-

60 concentration electrolyte (HCE) solvation structure while lowering viscosity and production

61 cost so that it can be applied to conventional cell geometries[27,28]. An HCE with 5M or a

62 higher salt concentration renders the inorganic-rich SEI formation with a higher mechanical

63 stability and stabilizes the LMA interface because of the lithium–ion–anion paired solvation

64 structure. Contact ion pair (CIP) and aggregate (AGG) solvation geometries are created

65 because there is no sufficient solvent molecule to solvate lithium–ions. However, the HCE

66 cannot be considered for practical applications because of its high viscosity and expensive

67 salt cost.

68 The addition of non-solvating cosolvents that enable the LHCE structure is a considerably

69 promising strategy because it can effectively lower the viscosity and cost of the HCE. The

70 design of ideal non-solvating cosolvents remains challenging because multiple components

71 need to be considered. Non-solvating cosolvents must not coordinate lithium–ions and be

72 inert to LMA for preserving the local solvation shell of HCE while being miscible with the

73 solvating solvent[29]. Conventionally, physicochemical parameters such as dielectric constant,

4

74   dipole moment, and calculated binding energy have been considered for predicting solvation

75   properties and miscibility with other solvents[14,16,30,31]. However, the behaviour of a cosolvent

76   mixed with multiple components in the electrolyte deviates from that of the pure form[32]. The

77   binding energy of the solvent-lithium–ion pair calculated by density functional theory (DFT)

78   is limited to local interactions, and it is less accurate at predicting the complex solvation

79   energetics in real electrolytes (**Figure 1c-d, inset**)[33]**.** The dipole moment and dielectric

80   constant, which only capture the polarity properties of the pure component, fail to represent

81   either the solvation ability or miscibility with the solvating solvent and concentrated salts in

82   the ensemble (**Figure S1c-d**)[31,34].

Figure 1. (**a**) HBA basicity vs. E_T^N (normalized transition energy) two-dimensional plot of each solvent. (**b**) Raman peak deconvolution for TFSI⁻ shift of electrolytes containing

86 different cosolvents (EC/DEC:cosolvent = 1:2). (**c**) Correlation between average CE and
87 HBA basicity. The average CE was obtained using an Aurbach method. The inset
88 demonstrates the correlation between the average CE and binding energy. (**d**) Correlation
89 between the Raman deconvolution result and HBA basicity. The inset demonstrates the
90 correlation between the Raman deconvolution result and binding energy. (**e**) Schematic of
91 HBA measurement using two different dyes. (**f**) Schematic of E_T^N (normalized transition
92 energy) measurement.

93

94 For example, the dielectric constant and dipole moment of tetrahydrofuran are 7.6 and 1.63D,

95 respectively; the values of 1,2-difluorobenzene are 14.26 and 2.53D, respectively. Despite the

96 higher values, the solvating property of 1,2-difluorobenzene is lower than that of

97 tetrafydrofuran[14,35]. Thus, a new paradigm of solvent descriptors that considers mutual

98 interaction with other components in the electrolyte should be established for designing new-

99 class cosolvents [34,36,37].

100 We propose experimental methods to characterize lithium–ion solvation ability and

101 miscibility with other polar species in electrolytes spectroscopically. It is imperative to

102 measure the stabilization energy of a lithium–ion in a specific solvation structure to assess the

103 lithium–ion solvation ability. In order to mimic the phenomenon, we utilized dyes that form

104 solvation structures with a solvent of interest and enable the measurement of the degree of

105 stabilization. One dye contains a primary amine group (-NH$_2$) that forms a hydrogen bond

106 with the surrounding solvent molecules while the other one, with the tertiary amine group (-

107 N(CH$_2$CH$_3$)$_2$), does not form the hydrogen bond. The difference between the absorption

108 energies of the two dyes represents their stabilization energies when solvated in a solvent

109 through hydrogen bonding. The solvation around the hydrogen of the primary amine group

110 may be close to that around the lithium–ion. This analogy thus mirrors the stabilization

111 energy of a solvated lithium–ion in a specific solvent environment. The strong interaction

112 between the electrons of the solvent and the cation is analogous to the Lewis acid–base

interaction; therefore, we refer to the solvation ability of the solvent as Lewis basicity. The method is as follows:

(1) We measured the absorption energies of a dye with -NH_2 (4-nitroaniline, NA), which corresponds to an acid–base reaction between N-H in NA and a solvent, and the additional Van der Waals attraction.

(2) We measured the absorption energy of a dye with -$N(CH_2CH_3)_2$ (N,N-diethyl-4-nitroaniline, DA) in the solvent to assess the Van der Waals attraction between DA and solvent.

(3) We fit the absorption energies in (2) to a linear calibration curve of absorption energies between DA and NA in a non-polar solvent to simulate the absorption energy of NA in the absence of the acid–base interaction.

(4) The difference between the absorption energies measured in (1) and (3) produces β, which reflects the acid–base interaction between the NA and the solvent, while completely removing the Van der Waals effect (Refer to **Supplementary Note 2** for the detailed calculation)[38,39].

We show that β is highly correlated with the solvation structures characterized by Raman spectroscopy—a widely-used tool to assess the lithium–ion-anion-solvent coordination degree—by analysing 14 solvents mixed with 1M LiTFSI EC/DEC (EC/DEC: cosolvent = 1:2) (**S1a, S2**). The decrease in the β of the cosolvent raises AGG and CIP ratios of anions (TFSI⁻), which is the ideal geometry for LHCE (**Figure 1b, d, S3**)[40]. Therefore, the battery CE is more highly correlated with β (Pearson's r: −0.847) than the calculated binding energy (Pearson's r: 0.573); this proves that the basicity of the cosolvent is a critical descriptor in

135   LMA performance (**Figure 1c-d**). A widely adopted basicity parameter, the Gutmann donor

136   number, demonstrates lower correlation with the battery CE (Pearson's r: −0.728), which

137   supports that β is the better basicity parameter (**Supplementary Note 1, Figure S1b**). This

138   result can be attributed to the SbCl₅ Lewis acid being used to calculate the Gutmann donor

139   number that is considerably larger than the lithium–ion. [27].To the best of our knowledge, such

140   an exclusive effect of β on the solvation structure and battery performance is yet to be

141   established.

142   We propose another solvatochromic parameter, E_T^N, as a descriptor of miscibility because it

143   can directly measure the stabilization energy stemming from the intermolecular attraction

144   between the solvent and mixed probe molecules. Since miscibility is best defined by mixing

145   enthalpies of species in an ensemble, the experimentally characterized intermolecular forces

146   between two dissimilar species better represent the miscibility than the dielectric constant and

147   dipole moment of pure species (**Figure 1a, S1c-d, Supplementary Note 3**). Although these

148   parameters guide miscibility between dissimilar molecules based on conventional wisdom

149   (i.e., like-dissolves-like), it is clearly limited in precisely determining miscibility. Further,

150   E_T^N measures the absorption energy of the 2,6-Diphenyl-4-(2,4,6-triphenyl-1-pyridino)

151   phenolate (Reichardt's dye) when it is mixed in the solvent of our interest (**Figure 1f**)[41,42].

152   The ground state of the dye becomes more stabilized, and the absorption energy increases

153   when the polar solvent is attracted to the anionic phenolate part of the dye[43]. Thus, cosolvents

154   with high E_T^N warrant the strong attraction to a polar electrolyte, i.e., miscibility within the

155   system (**Figure 1a**).

156   We discover the most optimal physicochemical properties for ideal cosolvents essential for

157   the high LMA performance while establishing the correlation of LHCE performance with β

9

158 and E_T^N: a low β (< 0.2) and a medium-high E_T^N. For the non-fluorinated solvents to have

159 such properties, the resonance structure connected to the oxygen atom is introduced to endow

160 solvents with non-solvating, miscible characteristics. We determined three NFNSC—AN,

161 ethoxybenzene, and furan—based on our correlation results and the design rule.

162 Comparison with the non-resonant analogues—methoxycyclohexane (MeCyHx),

163 benzylmethyl ether (BzMe), and tetrahydrofuran (THF)—reveals that molecules with oxygen

164 lone-pair electron resonance structures (**Scheme 1**) show lower β values, higher average CEs,

165 and longer capacity retention compared to those with limited or no resonance structures

166 (**Scheme 2**) (**Figure 2a, c).**
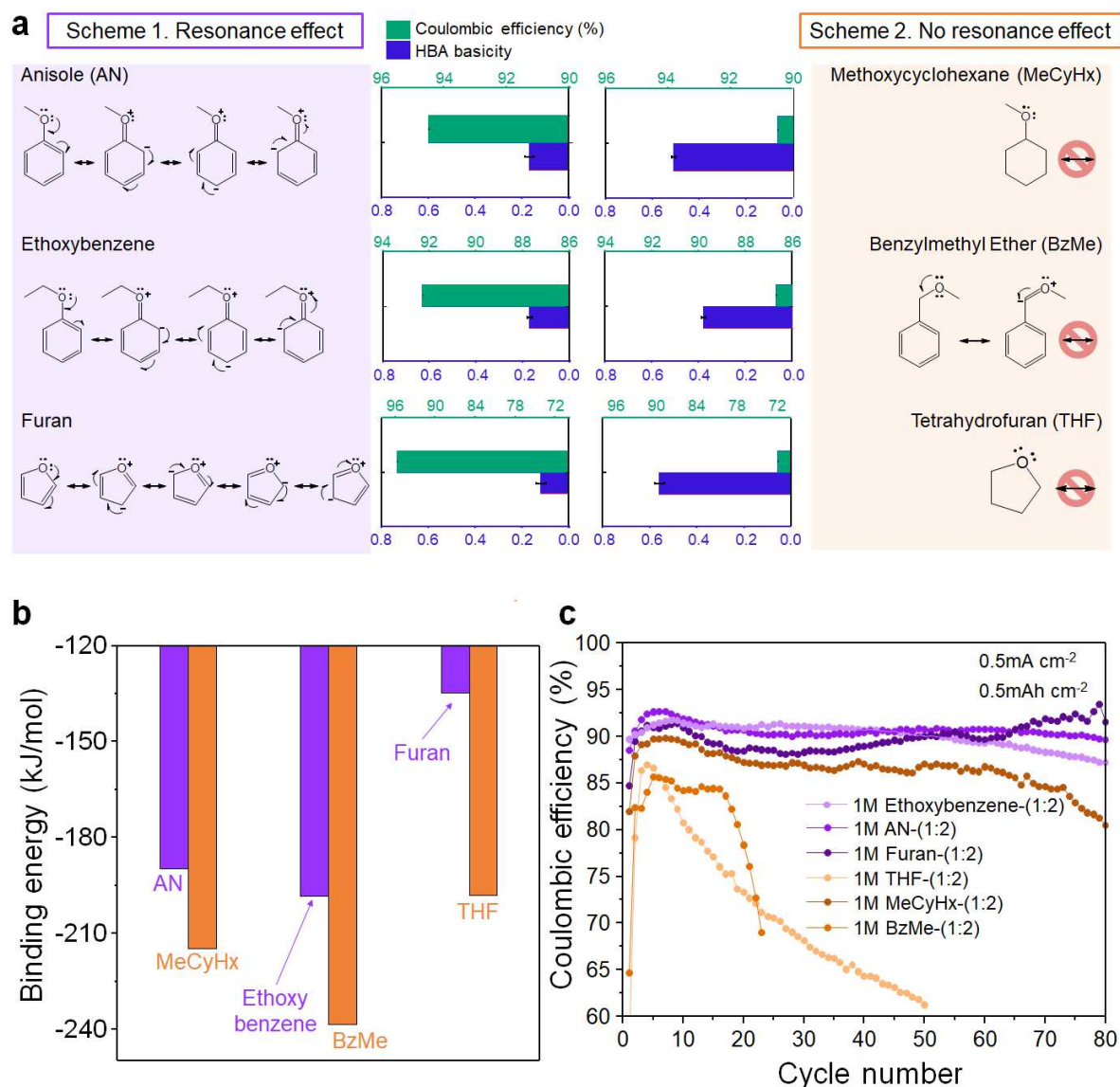
Figure 2. (**a**) Schematics of the resonance structures of organic compounds and corresponding CE and HBA basicity. (**b**) Calculated binding energies of lithium–ion with the oxygen atom of each compound. (**c**) Cycling performance of Li|Cu cell with different electrolytes at 0.5 mA cm^{-2} to 0.5 mAh cm^{-2}.

DFT calculations also suggest that the resonance can lower the binding energy to lithium–ion (**Figure 2b, Table S1**). In the calculation, the binding energies of the lithium–ion to the oxygen atom of AN, furan, and ethoxybenzene are significantly lower than those of analogous molecules despite their similar molecular structures except for the resonance capability.

176   Additional calculations were performed on several molecules with phenyl rings and oxygen

177   atoms (**Figure S7-8**). Comparing oxygen atoms connected directly to the phenyl ring and those

178   blocked by the methylene group, the former atoms exhibit lower binding energies

179   (**Supplementary Note 5**).

180

181   **Effect of AN on electrochemical performance of electrolytes**

182   We tested the electrochemical performance of the 1M LiTFSI EC/DEC (1M EC/DEC)

183   electrolyte, 5M LiTFSI EC/DEC (5M-HCE), and 1M LiTFSI EC/DEC:AN-(1:4) (1M AN-

184   (1:4)). The 1:4 ratio of EC/DEC to AN was selected to maintain the local concentration of

185   LiTFSI in EC/DEC as 5M and investigate the diluting effect of AN in the LHCE.

186   The TFSI$^-$ Raman peak shift of 1M AN-(1:4) was identical to that of the 5M-HCE and LiTFSI

187   salt, which confirm their identical solvation structures (**Figure 3a**). Further, the EC peak of

188   AN-(1:4) demonstrated a similar behaviour as that of 5M-HCE. Further deconvolution of the

189   TFSI$^-$ peak indicated that the CIP+AGG to SSIP peak ratio increases as the AN ratio increases

190   (**Figure S9**). Such LHCE solvation structure promotes the anion-derived SEI layer that was

191   observed from the XPS depth profile of the atomic ratio; F and S that comprise the inorganic

192   SEI layer were richer in 1M AN-(1:4) and 5M-HCE compared to 1M EC/DEC (**Figure S10-**

193   **11**).

194   The electrochemical performance using Li|Cu cell with 1M AN-(1:4) demonstrate

195   significantly improved cycle life and CE even in high current density and capacity (**Figure**

196   **3f, S12-13**). The superior performance of AN-containing electrolyte compared to 5M-HCE

197   and 1M EC/DEC can be attributed to the additional advantages of using non-solvating

198   cosolvents. In addition to 1M AN-(1:4) resembling the solvation structure of 5M-HCE, it has

199   a more compact SEI layer and minimized electrolyte decomposition. These were

200   characterized using scanning electron microscope (SEM) and electrochemical impedance

201   spectroscopy (EIS).

202
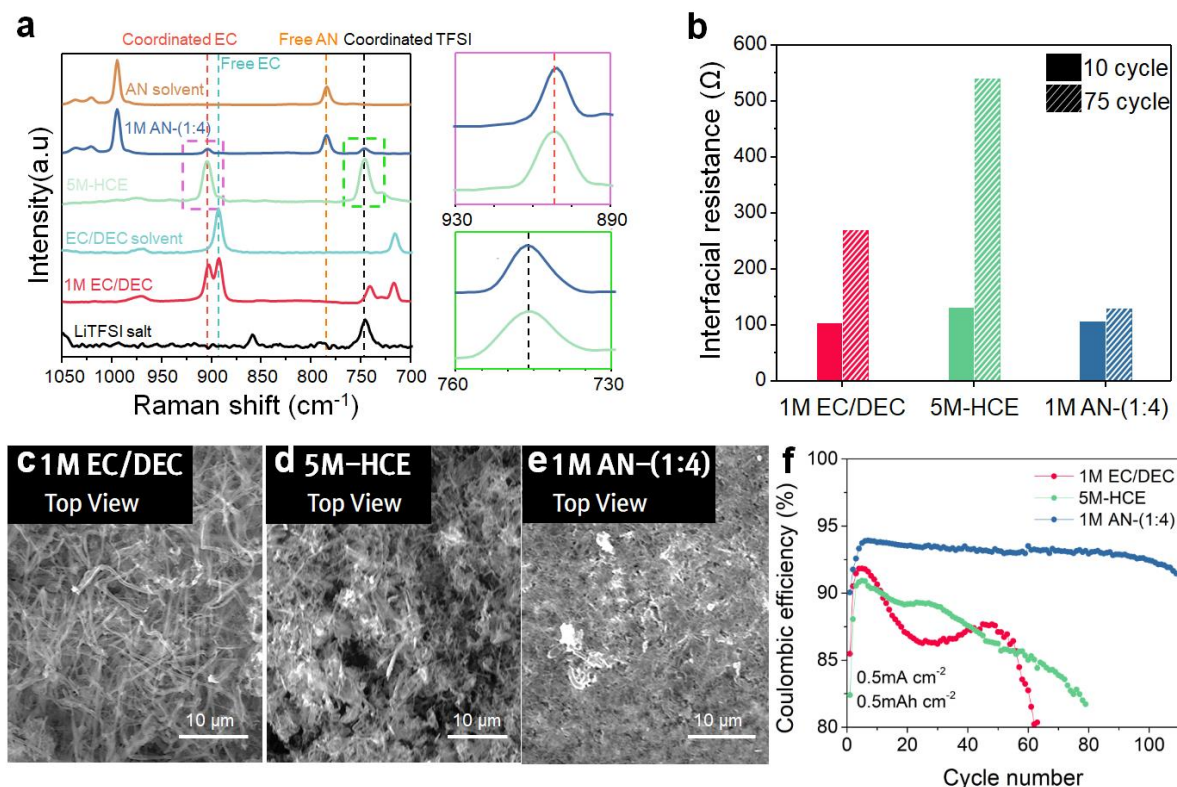
Figure 3. (**a**) Raman spectra of electrolytes and solvents containing LiTFSI, EC/DEC, and
AN. (**b**) EIS fitted interfacial resistance of different electrolytes at the 10th and 75th cycles.
Top-down SEM images of lithium deposition at (**c**) 1M EC/DEC, (**d**) 5M-HCE, and (**e**) 1M AN-
(1:4). (**f**) Cycling performance of Li|Cu cell with different electrolytes at 0.5 mA cm^{-2} to 0.5
mAh cm^{-2}.

208

209   The morphology of the lithium deposition of 1M AN-(1:4) examined using SEM exhibited a

210   significantly more compact lithium deposition morphology than the others (**Figure 3c-e,**

211   **S14**). Further, the cross-section SEM images indicated that 1M AN-(1:4) had both the

212   thinnest lithium metal layer with the smoothest surface (**Figure S15**). According to EIS, the

213   increment in the interfacial resistance from the 10th cycle to the 75th cycle is the smallest in

214 1M AN-(1:4) (**Figure 3b, S16-17**). This is further supported by Li 1s XPS depth profile of

215 the charged samples where the lithium metal peak of AN-(1:4) sample is observed to be

216 closer to the surface and online electrochemical mass spectrometry (OEMS) showing less

217 CO_2 and C_2H_4 gas formation in 1M AN-(1:4) (**Figure S18-19**).

218

Assessing practicality of NFNSC in LMA

220 Electrolyte salts and solvents were further optimized to improve cell performance. After

221 varying the salt concentration and volume ratio of AN, the 3M LiFSI DME:AN-(1:2) system

222 shows the highest performance (98.5% CE for 500 cycles) (**Figure 4a and Figure S20**). The

223 same electrolyte system was compared with the electrolytes without AN (3M LiFSI DME) and

224 HCE system (9M LiFSI DME). The Li|Cu cells containing 3M LiFSI DME:AN-(1:2)

225 performed the best even when the current density and capacity were raised to 2 mA cm^{-2} and

226 1 mAh cm^{-2}, respectively (99.1% CE for 270 cycles) (**Figure 4b**). The full cells with LFP

227 cathodes using thin foil lithium metal (20 μm) prove that the capacity retention and rate-

228 capability of AN are superior. 3M LiFSI DME:AN-(1:2) and 3M DME retain 85.4 % and 31.5 %

229 of its capacity at the 300th cycle and 36.9% and 10.1 % at 20 C compared to that at 0.2 C,

230 respectively (areal capacity: 1.2 mAh cm^{-2}) (**Figure S21-S23**). The Li|Cu cell of 3M LiFSI

231 DME:Furan-(1:2) maintains a high CE (99.0 %) for more than 1400 cycles (**Figure 4a**), and it

232 has the best reported cyclability among LMA LHCE to the best of our knowledge. The superior

233 performance of the furan containing electrolytes was maintained at high current density and

234 capacity (2 mA cm^{-2}, 1 mAhcm^{-2}) as it demonstrated 99.4 % of CE for more than 500 cycles

235 (**Figure 4b**).

236 Ionic conductivity significantly increases by more than one order with the addition of NFNSC

14

237 compared to that with 9M LiFSI DME (**Figure S24**)[15]. Comparing the interfacial resistance of

238 NFNSC containing electrolytes with that of 3M LiFSI DME by the EIS analysis, the smaller

239 SEI layer resistance of the cosolvent containing electrolytes at 1st and 55th deposition and the

240 smaller increase in the resistance confirm that the addition of cosolvents constructs a better

241 anode/electrolyte   interphase,   which   lowers   its   resistance   (**Figure   4c,   S25**).

242
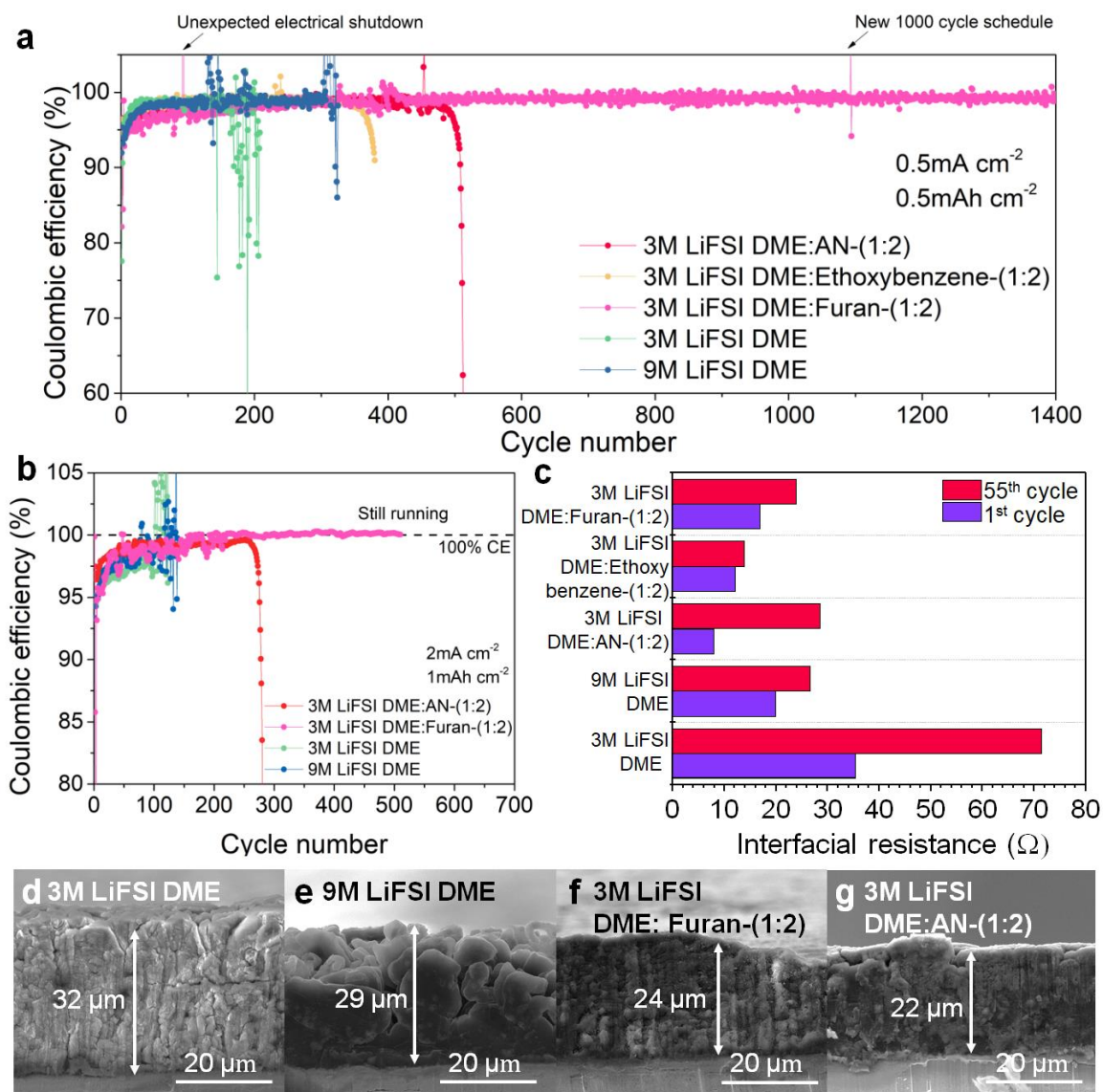
Figure 4. Cycling performance of Li|Cu cell with different electrolytes at (**a**) 0.5 mA cm^{-2} to 0.5
mAh cm^{-2}, and (**b**) 2 mA cm^{-2} to 1 mAh cm^{-2}. (**c**) Interfacial resistance of each electrolyte after
1st and 55th cycle obtained from the EIS. Cross-section SEM image of (**d**) 3M LiFSI DME, (**e**)
9M LiFSI DME, (**f**) 3M LiFSI DME:Furan-(1:2), and (**g**) 3M LiFSI DME:AN-(1:2), which each

247 having depths of 32 μm, 29 μm, 24 μm, and 22 μm, respectively.

248 Cross-section SEM data demonstrated that the deposited lithium metals in both 3M LiFSI

249 DME:AN-(1:2) and 3M LiFSI DME:Furan-(1:2) were more compact and thinner compared to

250 those in 3M and 9M LiFSI DME (**Figure 4d-g, S27**). Ethoxybenzene electrolyte (3M LiFSI

251 DME:ethoxybenzene-(1:2)) renders relatively thicker initial deposition, and it may be

252 responsible for the lowest cyclability among NFNSC-containing electrolytes (**Figure S25-26**).

253

254 **Quantification of cosolvents in electrolytes**

255 AN and furan-containing electrolytes demonstrated longer cycling than the reported cyclability

256 of DFB (350 cycles) and FB (500 cycles), which contain fluorine and induce the LiF formation

257 on LMA[14,15]. We attribute the long cyclabilities of our electrolytes to the high-energy position

258 of its LUMO. A LUMO level of a solvent is one of the dominating factors that determines the

259 performance of an electrolyte especially after extended cycling. A high LUMO level of the

260 solvent guarantees its high stability under reductive condition[44,45]. Our quantum chemical

261 calculations indicate that the LUMO level of AN is −0.543 eV and that of furan is −0.195 eV;

262 however, that of DFB is −0.950 eV, which is substantially lower (**Figure 5a**). The addition of

263 electronegative fluorine lowers the LUMO level, which aggravates the reduction and

264 decomposition of a cosolvent more preferably at the lithium anode interphases[14,15,20]. Such a

265 facile decomposition of a cosolvent not only leads to an electrolyte dry-up but may also

266 decrease partial concentration, which can result in the overall composition deviation from the

267 initially designed electrolyte with cycling[21]. We found that a decrease in the relative

268 composition of cosolvents can decrease the CE after extended cycling and induce battery

269 failure.
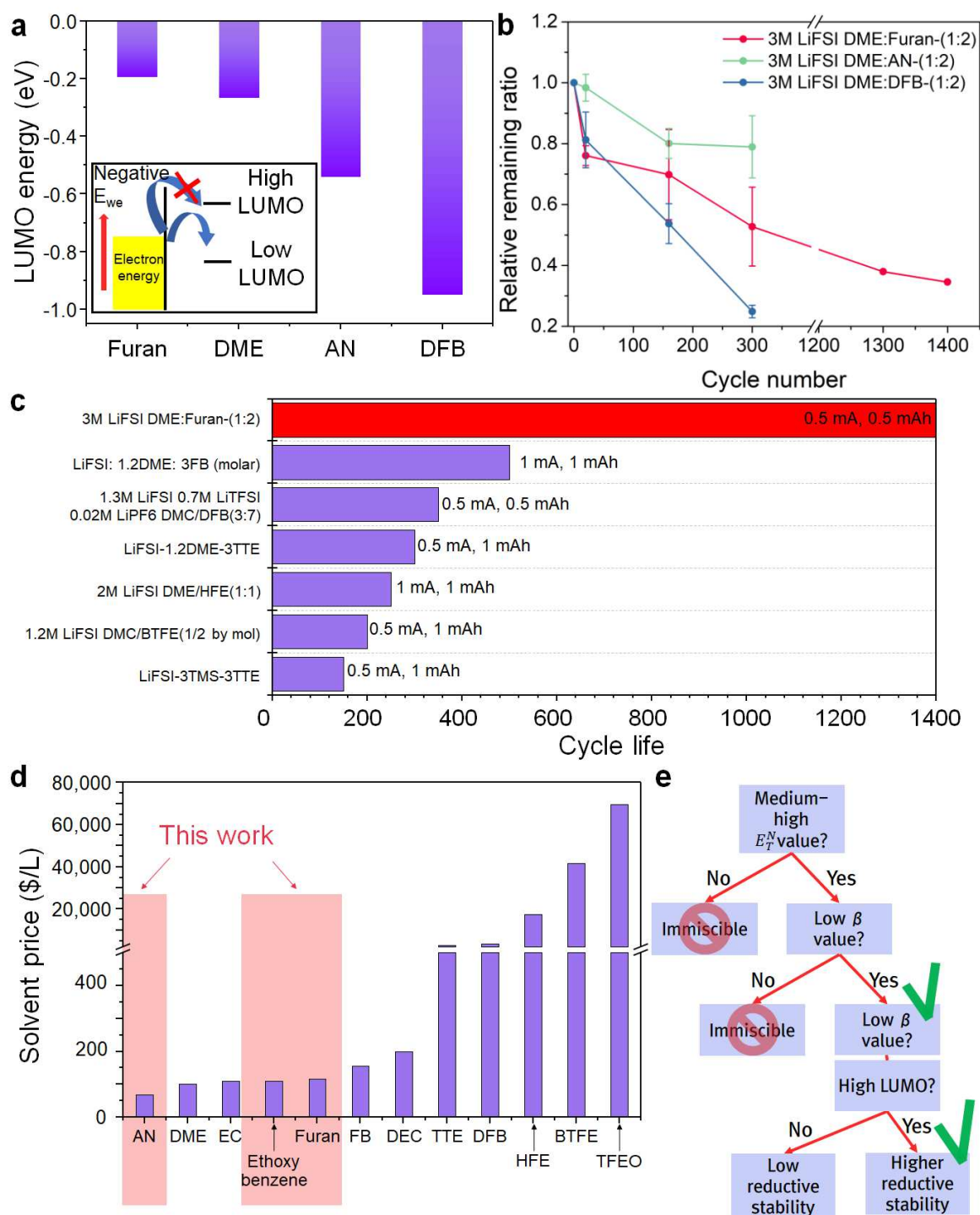
Figure 5. (**a**) Calculated LUMO energy of different solvents (Furan, DME, FB, and DFB). (**b**) Relative remaining ratio of each solvent after cycling the Li|Cu cells at 0.5 mA cm^{-2} to 0.5 mAh cm^{-2} for the designated cycle number. (**c**) Comparison of Li|Cu cell performance with various

275 cosolvents reported in previous studies. Their areal current density and areal capacity values
276 are indicated. (**d**) Comparison of the prices of (co)solvents commonly utilized in the LMA
277 electrolyte system. (**e**) A logic scheme for choosing an appropriate NFNSC.

278

279 Linear sweep voltammetry (LSV) of 1M DFB-(1:2) during initial charging exhibited additional

280 reduction peaks at a higher voltage (**Figure S28**), which suggest lower cathodic stability caused

281 by a low LUMO. In addition, ^{1}H-NMR spectroscopy was performed for electrolytes extracted

282 from the Li|Cu cells after cycling to quantify the concentration of the remaining cosolvents

283 (**Supplementary Note 7** for the specific method). The remaining quantity of furan and AN at

284 the extended cycles is higher than that of DFB with cycles (**Figure 5b**). About 35 % of furan

285 remained even after 1400 cycles, which is higher than the remaining ratios of DFB at 300

286 cycles. Our measurement does not detect the noticeable degradation of DME because of its

287 higher LUMO level compared to that of other cosolvents in this study; this suggests that the

288 degradation of cosolvents is responsible for the cycle capability (**Figure S29a**).

289 Overcoming the cycle capability of LMA longer than 500 cycles with a CE higher than 99.0%

290 has not been achieved before by any other conventional studies that rely on expensive

291 fluorinated cosolvents to the best of our knowledge[1,2,6,14,15,46]. Therefore, our design rule of the

292 cosolvent unlocks a route toward the LMA battery with an exceptionally long cycle life (**Figure**

293 **5c**). Along with the high CE and long cyclability, the cost of electrolytes has a major criteria in

294 assessing their practicality. The solvents investigated in this work are compared with other

295 cosolvents by their prices (**Figure 5d**). Many cosolvents that have been reported to date are

296 considerably more expensive, and this increases the battery production cost. Common,

297 fluorine-free organic compounds such as AN, furan, and ethoxybenzene are considerably

298 inexpensive and comparable to common solvents such as EC and DME in terms of cost.

299   Thus, we propose a logic scheme for selecting an appropriate non-solvating cosolvent for a

300   high-performance LMA electrolyte. The cosolvent should have a medium-high E_T^N to be

301   miscible with polar electrolytes, a low β value (< 0.2) to induce anion-coordinated solvation

302   structure, and a high LUMO to remain stable in a highly reductive condition (**Figure 5e**).

Conclusion

304   In this study, we proposed critical parameters for optimal non-solvating cosolvents and

305   correlated their effects with the electrochemical performance of various electrolytes. These

306   insights enable us to replace the conventional FNSC with NFNSC which show superior

307   cathodic stability confirmed by the long cyclability of 3M LiFSI DME:furan-(1:2) electrolyte.

308   This work represents a significant advancement in designing non-solvating cosolvents by

309   providing new means to tune the solvation ability of a molecule without aggravating the

310   reductive stability. Also, the design rule proposed here can be useful in determining solvation

311   ability and predicting the performance of newly-tested solvents in lithium metal battery

312   electrolyte. Overall, our proposal opens a new horizon for designing electrolytes for high

313   performance LMA.

Methods/Experimental Section

Materials and Electrolyte Preparation

316   LiTFSI (99.95%, trace metal basis), ethoxybenzene (99%), fluorobenzene (99%),

317   benzylmethyl ether (98%), dibenzyl ether (>98%), diphenyl ether (>99%), 1,2-

318   dimethoxyethane (99.5%, anhydrous, inhibitor free), ethylene carbonate (99%, anhydrous),

319   diethyl carbonate (>99%, anhydrous), dibutyl ether (99.30%, anhydrous), 1,3-dioxolane

320 (99.80%, anhydrous, contains ~75 ppm BHT as inhibitor, 99.8%), furan (>99%), 4-nitroaniline

321 (>99%) were purchased from Sigma-Aldrich. LiFSI (>98%), 1,2-difluorobenzene (>98%),

322 methoxycyclohexane (>98%), diisopropyl ether (>99%) were purchased from Tokyo Chemical

323 Industry Co., Ltd. AN (99%), methyl tert-butyl ether (HPLC grade, anhydrous),

324 tetrahydrofuran (99.8+%, anhydrous), 1,4-dioxane (anhydrous, 99.8%, stab. with 1-3ppm

325 BHT), LiCl (ultra dry, 99.995%) were purchased from Alfa Aesar. LiFSI (>99.97%) was

326 purchased from Chunbo. Deuterated dimethyl sulfoxide (DMSO-d^6, >99.8%) NMR solvent

327 was purchased from Deutero. N,N-Diethyl-4-nitroaniline (98%) was purchased from Combi-

328 Blocks. All solvents except EC were stored under a 4 Å molecular sieve (Alfa Aesar) for at

329 least two days and all electrolytes were prepared in an Ar-filled glove box. As the volumetric

330 ratio of EC/DEC was fixed to 1:1 for all the experiments, we do not explicitly indicate the ratio

331 for this mixture in the main article.

Calculating Solvatochromic β parameter

333 The β parameter was calculated based on the method proposed by Kamlet et al.[39] The

334 measurement was performed using a Shimadzu UV-2600 spectrophotometer. The spectral

335 range was 300–500 nm with a resolution of 0.1 nm. The final concentration of the dye was 1.0

336 × 10^{-4} M and each solvent was measured at least three times.

Electrochemical Testing

338 2032-type coin cells were assembled in an Ar-filled glove box. A Celgard 2320 microporous

339 membrane separator and 80 μL of electrolyte were used for integrating each cell. All cycling

340 experiments were performed at 25 °C using a WBCS3000L battery cycler (WonATech). Prior

341 to any cycling experiment, the Li|Cu cells were rested for 3 h at the OCV and then cycled at

342 the predetermined areal current and capacity. The cut-off voltage for each cycle was set to 1 V

343 (vs. Li/Li$^+$). The EIS and cyclic voltammetry (CV) were performed using VSP-300 (BioLogic)

344 in Li|Cu asymmetric cells. Both were measured at room temperature and rested for 30 seconds

345 at OCV before the measurement. The EIS measurements were conducted after the discharging

346 cycle. The frequency range was from 100 kHz to 0.1 Hz with a 10 mV amplitude.

347 **Characterization**

348 Cells were disassembled in an Ar-filled glove box. The electrodes were washed with the DEC

349 or DME solvent and dried under vacuum.

350 SEM (MIRA3 XMH, TESCAN) was used for morphology characterization. Loaded SEM

351 samples were directly placed into the chamber to minimize air contact. The accelerating voltage

352 was set to 15 kV.

353 The chemical compositions and bonding characteristics of the SEI layers were analysed using

354 XPS (Thermo VG Scientific (Sigma Probe, Mg Kα source)) and all peaks were fitted according

355 to the C-C bond 284.8 eV reference peak. For the survey scan, a 1.0 eV step size was used, and

356 a 0.1 eV step size was used for the high-resolution scans for all elements.

357 The coordination structure of various electrolytes was studied by Raman spectroscopy using

358 an inVia Raman Microscope (Renishaw) with an exciting laser of 514 nm. The peak

359 deconvolution of the obtained spectra was performed with a Gaussian function. For each

360 electrolyte, at least three spectra were reproduced on different days. The deconvoluted peak

361 ratios are the average values and the error bar is the 95 % confidential interval.

362 For the co-solvent and salt quantification, Li|Cu coin cells containing 40 μL of electrolytes

363 were cycled for specific cycles at 0.5 mA cm^{-2} to 0.5 mAh cm^{-2}. All coin cell parts were

364 disassembled and placed in a PTFE vial with 1 mL of DMSO-d$_6$. 20 μL of EC was used as an

365 internal standard for ^{1}H NMR. The vials were shaken for 5 min[47]. The ^{1}H NMR was performed

366 using 500 MHz NMR (Varian 500). Peak deconvolution was performed with Mestrenova

367 software using the Lorentzian fit method. This process was repeated at least three times for

368 each sample.

369 **Computational Details**

370 Quantum chemical calculations were performed with the Gaussian 16, Revision A.03 program

371 using the density functional theory (DFT) B3LYP functional using Grimme Dispersion (D3BJ)

372 and ultrafine integration[48,49]. Structure optimization was performed with the cc-pVTZ basis set

373 and a frequency calculation was performed to verify the absence of imaginary frequencies.

374 Single-point energy calculations were performed with the aug-cc-pVQZ basis set. From the

375 obtained structures, the binding energies and LUMO energy levels were obtained.

376

Acknowledgements

Author Contributions

388 J.M., D.K., and J.L. conceived the project and designed the experiments. J.M., D.K. did the

389 Li|Cu electrochemical testing and NMR spectroscopy. L.B. did the computational calculations.

390 M.S. and D.W. did the OEMS experiments. J.Y. and J.C. conducted the full-cell experiments.

391 J.Y. did the SEM and XPS characterizations. D.K. did the Raman experiment. J.Y. and D.K.

392 co-wrote the manuscript. All the authors discussed the results and commented on the

393 manuscript.

394

Reference

396 1. Chen, S. *et al.* High-Voltage Lithium-Metal Batteries Enabled by Localized High-Concentration

397   Electrolytes. *Adv. Mater.* **30**, 1706102 (2018).

398 2. Ren, X. *et al.* Localized High-Concentration Sulfone Electrolytes for High-Efficiency Lithium-

399   Metal Batteries. *Chem* **4**, 1877–1892 (2018).

400 3. Chen, J. *et al.* Highly Reversible Lithium-Metal Anode and Lithium–Sulfur Batteries Enabled by

401   an Intrinsic Safe Electrolyte. *ACS Appl. Mater. Interfaces* **11**, 33419–33427 (2019).

402   4.   Takada, K., Yamada, Y. & Yamada, A. Optimized Nonflammable Concentrated Electrolytes by

403   Introducing a Low-Dielectric Diluent. *ACS Appl. Mater. Interfaces* **11**, 35770–35776 (2019).

404   5.   Han, S. Structure and dynamics in the lithium solvation shell of nonaqueous electrolytes. *Sci.*

405   *Rep.* **9**, 5555 (2019).

406   6.   Ren, X. *et al.* Enabling High-Voltage Lithium-Metal Batteries under Practical Conditions. *Joule* **3**,

407   1662–1676 (2019).

408   7.   Xia, J. *et al.* Fluorinated electrolyte for 4.5 V Li(Ni0.4Mn0.4Co0.2)O2/graphite Li-ion cells. *J. Power*

409   *Sources* **307**, 340–350 (2016).

410   8.   Suo, L. *et al.* Fluorine-donating electrolytes enable highly reversible 5-V-class Li metal batteries.

411   *Proc. Natl. Acad. Sci.* **115**, 1156–1161 (2018).

412   9.   Lin, D., Liu, Y. & Cui, Y. Reviving the lithium metal anode for high-energy batteries. *Nat.*

413   *Nanotechnol.* **12**, 194–206 (2017).

414   10. Cheng, X.-B., Zhang, R., Zhao, C.-Z. & Zhang, Q. Toward Safe Lithium Metal Anode in

415   Rechargeable Batteries: A Review. *Chem. Rev.* **117**, 10403–10473 (2017).

416   11. Wang, H., Liu, Y., Li, Y. & Cui, Y. Lithium Metal Anode Materials Design: Interphase and Host.

417   *Electrochem. Energy Rev.* **2**, 509–517 (2019).

418   12. Li, T., Zhang, X.-Q., Shi, P. & Zhang, Q. Fluorinated Solid-Electrolyte Interphase in High-Voltage

419   Lithium Metal Batteries. *Joule* **3**, 2647–2661 (2019).

420   13. He, M., Guo, R., Hobold, G. M., Gao, H. & Gallant, B. M. The intrinsic behavior of lithium fluoride

421   in solid electrolyte interphases on lithium. *Proc. Natl. Acad. Sci.* **117**, 73–79 (2020).

422   14. Yoo, D., Yang, S., Kim, K. J. & Choi, J. W. Fluorinated Aromatic Diluent for High-Performance

423   Lithium Metal Batteries. *Angew. Chem. Int. Ed.* **59**, 14869–14876 (2020).

424   15. Jiang, Z. *et al.* Fluorobenzene, A Low-Density, Economical, and Bifunctional Hydrocarbon

425   Cosolvent for Practical Lithium Metal Batteries. *Adv. Funct. Mater.* **31**, 2005991 (2021).

426   16. Ding, J.-F. *et al.* Non-Solvating and Low-Dielectricity Cosolvent for Anion-Derived Solid

427   Electrolyte Interphases in Lithium Metal Batteries. *Angew. Chem. Int. Ed.* anie.202101627 (2021)

428   doi:10.1002/anie.202101627.

429   17. Su, C., He, M., Amine, R. & Amine, K. A Selection Rule for Hydrofluoroether Electrolyte Cosolvent:

430   Establishing a Linear Free-Energy Relationship in Lithium–Sulfur Batteries. *Angew. Chem. Int. Ed.*

431   **58**, 10591–10595 (2019).

432   18. Abdou, H. E., Mohamed, A. A., López-de-Luzuriaga, J. M., Monge, M. & Fackler, J. P. Fine-Tuning

433   the Luminescence and HOMO–LUMO Energy Levels in Tetranuclear Gold(I) Fluorinated

434   Amidinate Complexes. *Inorg. Chem.* **51**, 2010–2015 (2012).

435   19. Zhang, M., Guo, X., Zhang, S. & Hou, J. Synergistic Effect of Fluorination on Molecular Energy

436   Level Modulation in Highly Efficient Photovoltaic Polymers. *Adv. Mater.* **26**, 1118–1123 (2014).

437   20. Cao, X. *et al.* Monolithic solid–electrolyte interphases formed in fluorinated orthoformate-based

438   electrolytes minimize Li depletion and pulverization. *Nat. Energy* **4**, 796–805 (2019).

439   21. Jung, R. *et al.* Consumption of Fluoroethylene Carbonate (FEC) on Si-C Composite Electrodes

440	for Li-Ion Batteries. *J. Electrochem. Soc.* **163**, A1705–A1716 (2016).

441	22. Wang, A., Kadam, S., Li, H., Shi, S. & Qi, Y. Review on modeling of the anode solid electrolyte

442	interphase (SEI) for lithium-ion batteries. *Npj Comput. Mater.* **4**, 15 (2018).

443	23. Niu, C. *et al.* Balancing interfacial reactions to achieve long cycle life in high-energy lithium

444	metal batteries. *Nat. Energy* **6**, 723–732 (2021).

445	24. Niu, C. *et al.* High-energy lithium metal pouch cells with limited anode swelling and long stable

446	cycles. *Nat. Energy* **4**, 551–559 (2019).

447	25. Subramanian, M. A. A 'Greener' Synthetic Route for Fluoroaromatics via Copper (II) Fluoride.

448	*Science* **297**, 1665–1665 (2002).

449	26. Kyzer, J. L. & Martens, M. Metabolism and Toxicity of Fluorine Compounds. *Chem. Res. Toxicol.*

450	**34**, 678–680 (2021).

451	27. Yamada, Y. & Yamada, A. Review—Superconcentrated Electrolytes for Lithium Batteries. *J.*

452	*Electrochem. Soc.* **162**, A2406–A2423 (2015).

453	28. Yamada, Y., Wang, J., Ko, S., Watanabe, E. & Yamada, A. Advances and issues in developing salt-

454	concentrated battery electrolytes. *Nat. Energy* **4**, 269–280 (2019).

455	29. Cao, X., Jia, H., Xu, W. & Zhang, J.-G. Review—Localized High-Concentration Electrolytes for

456	Lithium Batteries. *J. Electrochem. Soc.* **168**, 010522 (2021).

457	30. Yao, Y. *et al.* Regulating Interfacial Chemistry in Lithium-Ion Batteries by a Weakly Solvating

458	Electrolyte**. *Angew. Chem. Int. Ed.* **60**, 4090–4097 (2021).

459   31. Chernyak, Y. Dielectric Constant, Dipole Moment, and Solubility Parameters of Some Cyclic Acid

460   Esters. *J. Chem. Eng. Data* **51**, 416–418 (2006).

461   32. Reichardt, C. *et al.* Solute/solvent interactions and their empirical determination by means of

462   solvatochromic dyes. *Pure Appl. Chem.* **65**, 2593–2601 (1993).

463   33. Bezabh, H. K. *et al.* Roles of film-forming additives in diluted and concentrated electrolytes for

464   lithium metal batteries: A density functional theory-based approach. *Electrochem. Commun.*

465   **113**, 106685 (2020).

466   34. Zhuang, B., Ramanauskaite, G., Koa, Z. Y. & Wang, Z.-G. Like dissolves like: A first-principles

467   theory for predicting liquid miscibility and mixture dielectric constant. *Sci. Adv.* **7**, eabe7275

468   (2021).

469   35. Obukata, T., Yamada, Y. & Yamada, A. Controlling the coordination states of electrolyte solutions

470   for reversible lithium metal plating/stripping. 1.

471   36. Aldeghi, M., Heifetz, A., Bodkin, M. J., Knapp, S. & Biggin, P. C. Accurate calculation of the

472   absolute free energy of binding for drug molecules. *Chem. Sci.* **7**, 207–218 (2016).

473   37. Chaban, V. Competitive solvation of (bis)(trifluoromethanesulfonyl)imide anion by acetonitrile

474   and water. *Chem. Phys. Lett.* **613**, 90–94 (2014).

475   38. Nigam, S. & Rutan, S. Principles and Applications of Solvatochromism. *Appl. Spectrosc.* **55**,

476   362A-370A (2001).

477   39. Kamlet, M. J. & Taft, R. W. The solvatochromic comparison method. I. The .beta.-scale of solvent

478   hydrogen-bond acceptor (HBA) basicities. *J. Am. Chem. Soc.* **98**, 377–383 (1976).

479   40. Yamada, Y. *et al.* Unusual Stability of Acetonitrile-Based Superconcentrated Electrolytes for Fast-

480   Charging Lithium-Ion Batteries. *J. Am. Chem. Soc.* **136**, 5039–5046 (2014).

481   41. Nigam, S. & Rutan, S. Principles and Applications of Solvatochromism. *Appl. Spectrosc.* **55**,

482   362A-370A (2001).

483   42. Reichardt, C. Solvatochromic Dyes as Solvent Polarity Indicators. *Chem. Rev.* **94**, 2319–2358

484   (1994).

485   43. Dimroth, K., Reichardt, C., Siepmann, T. & Bohlmann, F. Über Pyridinium-N-phenol-betaine und

486   ihre Verwendung zur Charakterisierung der Polarität von Lösungsmitteln. *Justus Liebigs Ann.*

487   *Chem.* **661**, 1–37 (1963).

488   44. Xu, K. Electrolytes and Interphases in Li-Ion Batteries and Beyond. *Chem. Rev.* **114**, 11503–11618

489   (2014).

490   45. Borodin, O. Challenges with prediction of battery electrolyte electrochemical stability window

491   and guiding the electrode – electrolyte stabilization. *Curr. Opin. Electrochem.* **13**, 86–93 (2019).

492   46. Lin, S. & Zhao, J. Functional Electrolyte of Fluorinated Ether and Ester for Stabilizing Both 4.5 V

493       $LiCoO_2$ Cathode and Lithium Metal Anode. *ACS Appl. Mater. Interfaces* **12**, 8316–8323 (2020).

494   47. Louli, A. J. *et al.* Diagnosing and correcting anode-free cell failure via electrolyte and

495   morphological analysis. *Nat. Energy* **5**, 693–702 (2020).

496   48. Becke, A. D. Density-functional thermochemistry. III. The role of exact exchange. *J. Chem. Phys.*

497   **98**, 5648–5652 (1993).

498   49. Parr, R. G. & Yang, W. *Density-functional theory of atoms and molecules*. (Oxford Univ. Press

499   [u.a.], 1994).

500

Supplementary Files

This is a list of supplementary files associated with this preprint. Click to download.

- SupplementaryMaterialsfinal1028.pdf